Spin Dynamics in Hierarchical Black Hole Triples: Predicting Final Spin-Orbit Misalignment Angle From Initial Conditions

Yubo Su,[1] Dong Lai,[1] and Bin Liu[1]

[1]*Cornell Center for Astrophysics and Planetary Science, Department of Astronomy, Cornell University, Ithaca, NY 14853, USA*

ABSTRACT

Abstract

1. INTRODUCTION

As the LIGO/VIRGO collaboration continues to detect mergers of black hole (BH) binaries (e.g. Abbott et al. 2016, 2019), it is increasingly important to systematically study various formation channels of BH binaries and their observable signatures. The canonical channel consists of isolated binary evolution, in which mass transfer and friction in the common envelope phase cause the binary orbit to shrink sufficiently that it subsequently merges via emission of gravitational waves (GW) within a Hubble time (e.g. Lipunov et al. 1997, 2017; Podsiadlowski et al. 2003; Belczynski et al. 2010, 2016; Dominik et al. 2012, 2013, 2015) BH binaries formed via isolated binary evolution are generally expected to have small misalignment between the BH spin axis and the orbital angular momentum axis (Postnov & Kuranov 2019; Belczynski et al. 2020). On the other hand, various flavors of dynamical formation channels of BH binaries have also been studied. These involve either strong gravitational scatterings in dense clusters (e.g. Zwart & McMillan 1999; O'leary et al. 2006; Miller & Lauburg 2009; Banerjee et al. 2010; Downing et al. 2010; Ziosi et al. 2014; Rodriguez et al. 2015; Samsing & Ramirez-Ruiz 2017; Samsing & D'Orazio 2018; Rodriguez et al. 2018; Gondán et al. 2018) or more gentle "tertiary-induced mergers" (e.g. Blaes et al. 2002; Miller & Hamilton 2002; Wen 2003; Antonini & Perets 2012; Antonini et al. 2017; Silsbee & Tremaine 2016; Liu & Lai 2017, 2018; Randall & Xianyu 2018; Hoang et al. 2018). The dynamical formation channels generally produce BH binaries with misaligned spins.

Corresponding author: Yubo Su

yubosu@astro.cornell.edu

In some cases, GW observations of binary inspirals can put constraints on BH spins. Typically, spin constraints come in the form of two dimensionless mass-weighted combinations of the component BH spins: (i) the aligned spin parameter

$$\chi_{\rm eff} \equiv \frac{m_1 \cos \theta_{\rm s_1,l} + m_2 \cos \theta_{\rm s_2,l}}{m_1 + m_2} \qquad (1)$$

where $m_{1,2}$ are the masses of the BHs and $\theta_{\rm s_i,l}$ is the angle between the ith spin and the binary orbital angular momentum axis; and (ii) the perpendicular spin parameter (Schmidt et al. 2015)

$$\chi_{\rm p} \equiv \max \left\{ \chi_1 \sin \theta_{\rm s_1,l}, \frac{q\,(4q+3)}{4+3q} \chi_2 \sin \theta_{\rm s_2,l} \right\}. \qquad (2)$$

Many systems detected in the O1 and O2 observing runs have small $\chi_{\rm eff}$, which is consistent with either small or highly misaligned ($\theta_{\rm s_i,l} \approx 90°$) BH spins.

TODO Update this paragraph later with references. In the recent GW detection GW190521.1, the component BHs have dimensionless spins $\chi_{1,2} = S_{1,2}/M_{1,2}^2 \sim 0.7$, yet $\chi_{\rm eff} \approx 0$ while $\chi_{\rm p} \sim 1$. This requires both BH spins be misaligned with the orbital angular momentum, i.e. $\theta_{\rm s_i,l} \approx 90°$.

Liu & Lai (2017, 2018, hereafter LL17, LL18), and Liu et al. (2019) carried out a systematic study of binary BH mergers in the presence of a tertiary companion. LL17 pointed out the important effect of spin-orbit coupling (de-Sitter precession) in determining the final spin-orbit misalignment angles of BH binaries in triple systems. They considered binaries with sufficiently compact orbits (so that mergers are possible even without a tertiary) and showed that the combination of LK oscillations (induced by a modestly inclined tertiary) and spin-orbit coupling gives rise to a broad range of final spin-orbit misalignment in the merging binary BHs. We call

these mergers *LK-enhanced mergers*, as LK oscillations enhance the inspiral rate. LL18 considered the most interesting case of *LK-induced mergers*, in which an initially wide BH binary (too wide to merge in oscillation) is pushed to very large eccentricities (close to unity) by a highly inclined tertiary and merges within a few Gyrs. LL18 examined a wide range of orbital and spin evolution behaviors, and found that LK-induced mergers can sometimes yield a "90° attractor": when one component BH of the inner binary has initial spin-orbit misalignment angle $\theta_{sl}^i = 0$, it often evolves towards $\theta_{sl}^f = 90°$. They found that the attractor exists when (i) the LK-induced orbital decay is slow, and (ii) the octupole effect is unimportant. Fig. 1 gives an example of a system evolving towards this attractor, where θ_{sl} rapidly converges to $\approx 90°$ at late times in the bottom right panel. Fig. 2 shows how θ_{sl}^f varies when the initial inclination of the inner orbit I_0 (relative to the tertiary orbit) is varied. Note that for longer merger times, corresponding to I_0 farther from 90°, the final $\theta_{sl}^f \approx 90°$. In both of these plots, the tertiary's eccentricity is taken to be zero, for which octupole effects are negligible.

The physical origin of this 90° attractor is not well understood. LL18 proposed an explanation based on analogy with an adiabatic invariant in systems where the inner binary remains circular through the inspiral LL17. However, this analogy is not justified, as significant eccentricity excitation is a necessary ingredient in LK-induced mergers. In addition, the results in LL17 show no 90° attractor even though the orbital evolution is slow and regular.

In this paper, we study an analytic theory that reproduces the 90° attractor as well as its regime of validity. In Sections 2 and 3, we set up the relevant equations of motion for the orbital and spin evolution of the system. In Sections 4 and 5, we develop an analytic theory and compute its regime of validity for LK-induced mergers. In Section 6, we comment on the consistency of our results with LL17. We discuss and conclude in Section 7.

2. LK-INDUCED MERGERS: ORBITAL EVOLUTION

In this section we summarize the key features and relevant equations for LK-induced mergers to be used for our analysis in later sections. Consider a black hole (BH) binary with masses m_1 and m_2 having total mass m_{12}, reduced mass $\mu = m_1 m_2 / m_{12}$, semimajor axis a and eccentricity e. This inner binary orbits around a tertiary with mass m_3, semimajor axis a_3 and eccentricity e_3 in a hierachical configuration ($a_3 \gg a$). Unless explicitly stated, we assume $m_3 \gg m_1, m_2$ (so the tertiary is a supermassive black hole, or SMBH), although our analysis can be easily generalized to comparable masses. Then define the effective semimajor axis to be

$$\tilde{a}_3 \equiv a_3 \sqrt{1 - e_3^2}. \tag{3}$$
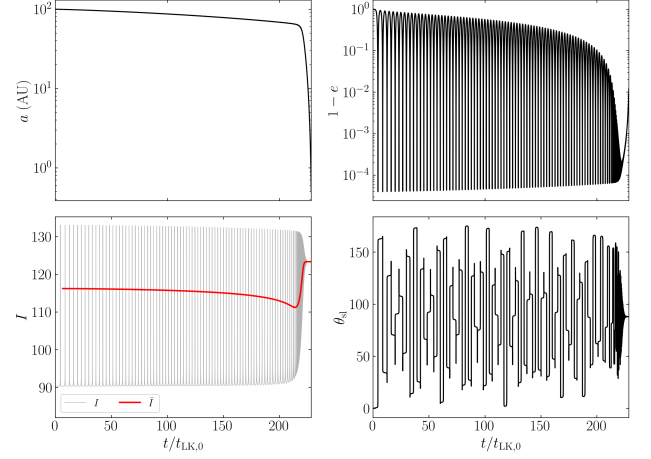
Figure 1. An example of the 90° attractor in LK-induced BH binary mergers. The four panes show the time evolution of the binary semi-major axis a, eccentricity e, inclination I [including an averaged $\bar{I}$ given by Eq. (33)], and spin-orbit misalignment angle θ_{sl}. The unit of time $t_{LK,0}$ is the LK timescale [Eq. (10)] evaluated for the initial conditions. The inner binary is taken to have $a = 100$ AU, $m_1 = 30 M_\odot$, $m_2 = 20 M_\odot$, $I_0 = 90.35°$, and $e_0 = 0.001$, while the tertiary SMBH has $a_3 = 2.2$ pc, $e_3 = 0$, $m_3 = 3 \times 10^7 M_\odot$, and initially $\theta_{sl}^i = 0$. It can be seen that θ_{sl}^f converges rapidly to $\sim 90°$ at the end of the simulation.
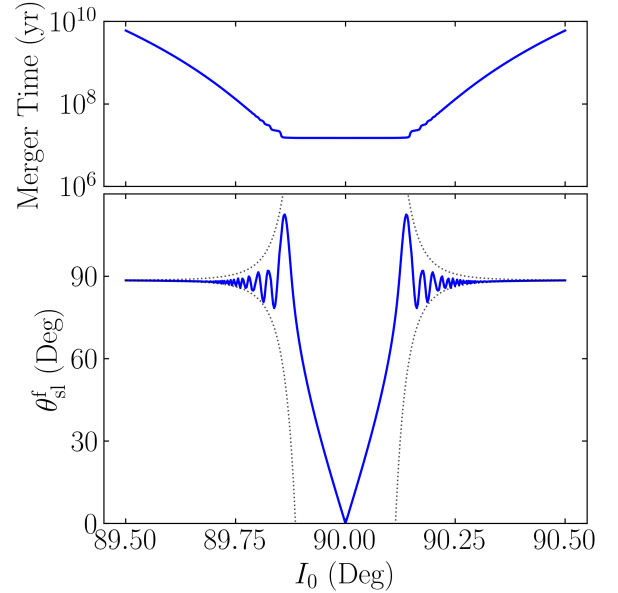
Figure 2. Plot of merger time of the inner binary and θ_{sl}^f for the fiducial parameters, with $\theta_{sl}^i = 0$ and using a restricted range of I_0 (analogous to the bottom-most panel in Fig. 3 of Liu & Lai 2018), where the blue line is taken from numerical simulations. It is clear that for I_0 sufficiently far from 90°, the resulting θ_{sl}^f are all quite near 90° (Liu & Lai 2018). The black dashed line shows Eq. (64), which predicts the deviation of θ_{sl} from the 90° attractor.

We denote the orbital angular momentum of the inner binary by $\mathbf{L} \equiv L\hat{\mathbf{L}}$ and the angular momentum of the binary relative to the SMBH as $\mathbf{L}_3 \equiv L_3\hat{\mathbf{L}}_3$. Since $L_3 \gg L$, we take $\mathbf{L}_3$ to be fixed.

The equations of motion governing the orbital elements a, e, Ω, I, ω (where Ω, I, ω are the longitude of the ascending node, inclination, and argument of periapsis respectively) of the inner binary are then (Peters 1964; Storch & Lai 2015; Liu & Lai 2018)

$$\frac{da}{dt} = \left(\frac{da}{dt}\right)_{\mathrm{GW}}, \tag{4}$$

$$\frac{de}{dt} = \frac{15}{8t_{\mathrm{LK}}} e j(e) \sin 2\omega \sin^2 I + \left(\frac{de}{dt}\right)_{\mathrm{GW}}, \tag{5}$$

$$\frac{d\Omega}{dt} = \frac{3}{4t_{\mathrm{LK}}} \frac{\cos I \left(5e^2 \cos^2 \omega - 4e^2 - 1\right)}{j(e)}, \tag{6}$$

$$\frac{dI}{dt} = \frac{15}{16} \frac{e^2 \sin 2\omega \sin 2I}{j(e)}, \tag{7}$$

$$\frac{d\omega}{dt} = \frac{3}{4t_{\mathrm{LK}}} \frac{2j^2(e) + 5\sin^2 \omega(e^2 - \sin^2 I)}{j(e)} + \Omega_{\mathrm{GR}}, \tag{8}$$

where we have defined

$$j(e) = \sqrt{1 - e^2}, \tag{9}$$

$$t_{\mathrm{LK}}^{-1} \equiv n \left(\frac{m_3}{m_{12}}\right) \left(\frac{a}{\tilde{a}_3}\right)^3,, \tag{10}$$

with $n \equiv \sqrt{Gm_{12}/a^3}$ the mean motion of the inner binary. The GR-induced apsidal precession of the inner binary is given by

$$\Omega_{\mathrm{GR}}(e) = \frac{3Gnm_{12}}{c^2 a j^2(e)}. \tag{11}$$

The dissipative terms due to gravitational radiation are

$$\left(\frac{da}{dt}\right)_{\mathrm{GW}} = -\frac{a}{t_{\mathrm{GW}}(e)}, \tag{12}$$

$$\left(\frac{de}{dt}\right)_{\mathrm{GW}} = -\frac{304}{15} \frac{G^3 \mu m_{12}^2}{c^5 a^4} \frac{1}{j^{5/2}(e)} \left(1 + \frac{121}{304}e^2\right), \tag{13}$$

where

$$t_{\mathrm{GW}}^{-1}(e) \equiv \frac{64}{5} \frac{G^3 \mu m_{12}^2}{c^5 a^4} \frac{1}{j^{7/2}(e)} \left(1 + \frac{73}{24}e^2 + \frac{37}{96}e^4\right). \tag{14}$$

Fig. 1 depicts an example of LK-induced mergers as cacluated using the above equations. We adopt the following fiducial parameters: the inner binary has $a = 100$ AU, $m_1 = 30M_\odot$, $m_2 = 20M_\odot$, initial $e_0 = 0.001$, and initial $I_0 = 90.35°$. We take the SMBH tertiary companion to have $m_3 = 3 \times 10^7 M_\odot$ and $\tilde{a}_3 = 4.5 \times 10^5$ AU $= 2.2$ pc. Note that these parameters give the same t_{LK} as Fig. 4 of LL18. We refer to this as the fiducial parameter regime, and our

analysis in later sections will be based on this example unless otherwise noted.

We summarize a few key analytical properties of this orbital evolution below:

- Neglecting GR effects (GW radiation and apsidal precession), the above equations describe periodic oscillations in e and I. There are two conserved quantities, the total angular momentum $\mathbf{L}_3 + \mathbf{L}$ and the "Kozai constant" (Lidov 1962; Kozai 1962):

$$K \equiv j(e) \cos I. \tag{15}$$

This implies that e is a function of ω only (Kinoshita 1993; Storch & Lai 2015).

Note that an eccentricity maxiumum occurs every half-period of ω, at $\omega = \pi/2$ and $\omega = 3\pi/2$ (Kinoshita 1993; Storch & Lai 2015). It is most convenient to define the LK period P_{LK} as the *half*-period of ω, and the corresponding frequency Ω_{LK}:

$$\pi = \int_0^{P_{\mathrm{LK}}} \frac{d\omega}{dt} \, dt, \tag{16}$$

$$\Omega_{\mathrm{LK}} \equiv \frac{2\pi}{P_{\mathrm{LK}}}. \tag{17}$$

The conservation laws above can be combined to calculate the maximum eccentricity as a function of I. If the minimum eccentricity is negligible and the inclination at the start of the LK cycle is I_0, then

$$e_{\mathrm{max}} \equiv \sqrt{1 - \frac{5}{3} \cos^2 I_0}. \tag{18}$$

Note that these results assume $L_3 \gg L$ and that both octupole and GR effects are negligible; see LL18 for generalized forms of the above results.

Finally, when $e_{\mathrm{min}} \ll e_{\mathrm{max}}$, the binary spends a fraction $\sim j(e_{\mathrm{max}})$ of the LK cycle near $e \simeq e_{\mathrm{max}}$ (Anderson et al. 2016).

- When GR effects are considered, the system gradually coalesces due to GW radiation, primarily in the $j(e_{\mathrm{max}})P_{\mathrm{LK}}$ window at eccentricity maxima. During this process, there are three competing timescales: (i) Ω precession driven by the tertiary ($\sim t_{\mathrm{LK}}$), (ii) apsidal precession due to post-Newtonian effects ($\sim \Omega_{\mathrm{GR}}^{-1}(e_{\mathrm{max}})/j(e_{\mathrm{max}})$), and (iii) orbital decay due to GW radiation ($\sim t_{\mathrm{GW}}(e_{\mathrm{max}})/j(e_{\mathrm{max}})$). At early times, (i) is the shortest, but as a decreases, (ii) and (iii) become dominant and eccentricity oscillations become suppressed, which we term "eccentricity freezing". We consider the two conditions under which this happens.

Apsidal precession becomes important when $\Omega_{\rm GR}$ is the dominant contribution in Eq. (8). Quantitatively, this occurs when

$$\frac{\epsilon_{\rm GR}}{j(e_{\rm max})} \gg 1, \qquad (19)$$

where we define

$$\epsilon_{\rm GR} \equiv \frac{3Gm_{12}^2 \tilde{a}_3^3}{c^2 m_3 a^4}. \qquad (20)$$

GW radiation can also inhibit eccentricity oscillations when $t_{\rm LK} j(e) \gtrsim t_{\rm GW}(e)$ [see Eq. (5)]. In order for GW radiation to be the dominant cause of eccentricity freezing, we require

$$1 \lesssim \frac{t_{\rm GW}^{-1}(e)}{\Omega_{\rm GR}} \sim \left(\frac{Gm_{12}}{a j^2(e) c^2}\right)^{3/2} \frac{1}{1 - e^2}, \qquad (21)$$

$$\sim \left(\frac{v_p}{c}\right)^3 \frac{1}{1 - e^2}, \qquad (22)$$

where v_p is the pericenter velocity of the inner binary. Since $v_p/c \ll 1$, we find that apsidal precession is usually more effective at freezing the eccentricity.

The behavior of a, e, and I for a characteristic LK-induced merger can be seen in Fig. 1. At early times, e and I have large oscillations while a slowly decreases. At later times, e and I stop oscillating as apsidal precession freezes the eccentricity, and both a and e decrease under GW radiation. Since $P_{\rm LK}$ is defined as the half-period in ω, $\Omega_{\rm LK}$ asymptotes to $\Omega_{\rm GR}$ at late times even though the eccentricity is frozen (bottom right panel of Fig. 1).

3. SPIN DYNAMICS: EQUATIONS

We are interested in the spin orientations of the inner BHs at merger as a function of initial conditions. Since they evolve independently to leading post-Newtonian order, we focus on the dynamics of $\hat{\mathbf{S}}_1 = \hat{\mathbf{S}}$, the spin vector of m_1. Since the spin magnitude does not enter into the dynamics, we write $\mathbf{S} \equiv \hat{\mathbf{S}}$ for brevity (i.e. $\mathbf{S}$ is a unit vector). Neglecting spin-spin interactions, $\mathbf{S}$ undergoes de Sitter precession about $\mathbf{L}$ as

$$\frac{d\mathbf{S}}{dt} = \Omega_{\rm SL} \hat{\mathbf{L}} \times \mathbf{S}, \qquad (23)$$

with

$$\Omega_{\rm SL} = \frac{3Gn(m_2 + \mu/3)}{2c^2 a j^2(e)}. \qquad (24)$$

In the presence of a tertiary companion, the orbital axis $\hat{\mathbf{L}}$ of the inner binary precesses around $\hat{\mathbf{L}}_3$ with rate $d\Omega/dt$ and nutates with varying I [see Eqs. (6) and (7)]. To analyze the

dynamics of the spin vector, we go to co-rotating frame with $\hat{\mathbf{L}}$ about $\hat{\mathbf{L}}_3$, where Eq. (23) becomes

$$\left(\frac{d\mathbf{S}}{dt}\right)_{\rm rot} = \mathbf{\Omega}_{\rm e} \times \mathbf{S}, \qquad (25)$$

where we have defined an effective rotation vector

$$\mathbf{\Omega}_{\rm e} \equiv \Omega_{\rm L} \hat{\mathbf{L}}_3 + \Omega_{\rm SL} \hat{\mathbf{L}}, \qquad (26)$$

with [see Eq. (6)]

$$\Omega_{\rm L} \equiv -\frac{d\Omega}{dt}. \qquad (27)$$

In this rotating frame, the plane spanned by $\hat{\mathbf{L}}_3$ and $\hat{\mathbf{L}}$ is constant in time, only the inclination angle I can vary.

3.1. Nondissipative Dynamics

We first consider the limit where dissipation via GW radiation is completely neglected ($t_{\rm GW}(e) \to \infty$). Then $\mathbf{\Omega}_{\rm e}$ is exactly periodic with period $P_{\rm LK}$ [see Eq. (16)] We can rewrite Eq. (25) in Fourier components

$$\left(\frac{d\mathbf{S}}{dt}\right)_{\rm rot} = \left[\overline{\mathbf{\Omega}}_{\rm e} + \sum_{N=1}^{\infty} \mathbf{\Omega}_{\rm eN} \cos\left(N\Omega_{\rm LK} t\right)\right] \times \mathbf{S}. \qquad (28)$$

We write $\overline{\mathbf{\Omega}}_{\rm e} \equiv \mathbf{\Omega}_{\rm e0}$ for convenience, where the bar denotes an average over a LK cycle. We adopt the convention where $t = 0$ is the time of maximum eccentricity of the LK cycle.

This system superficially resembles that studied in Storch & Lai (2015) (SL15), who studied the dynamics of the spin axis of a star when driven by a giant planet undergoing LK oscilations. In their system, the spin-orbit coupling arises from Newtonian interaction between the planet ($M_{\rm p}$) and the rotation-induced stellar quadrupole ($I_3 - I_1$), and the spin precession frequency is

$$\Omega_{\rm SL}^{\text{(Newtonian)}} = -\frac{3GM_{\rm p}(I_3 - I_1)}{2a^3 j^3(e)} \frac{\cos\theta_{\rm sl}}{S}. \qquad (29)$$

SL15 showed that under some conditions that depend on a dimensionless adiabaticity parameter (roughly the ratio between the magnitudes of $\Omega_{\rm SL}^{\text{(Newtonian)}}$ and $\Omega_{\rm L}$ when factoring out the eccentricity and obliquty dependence), the stellar spin axis can vary chaotically. One strong indicator of chaos in their study is the presence of fine structure in a bifurcation diagram [Fig. 1 of Storch & Lai (2015)] that shows the values of the spin-orbit misalignment angle $\theta_{\rm sl}$ when varying system parameters in the "transadiabatic" regime, where the adiabaticity parameter crosses 1.

To generate an analogous bifurcation diagram for our problem, we consider a sample system with $m_{12} = 60M_\odot$, $m_3 = 3 \times 10^7 M_\odot$, $a = 0.1$ AU, $e_0 = 10^{-3}$, $I_0 = 70°$, $a_3 = 300$ AU, $e_3 = 0$, and initial condition $\theta_{\rm sl} = 0$. We
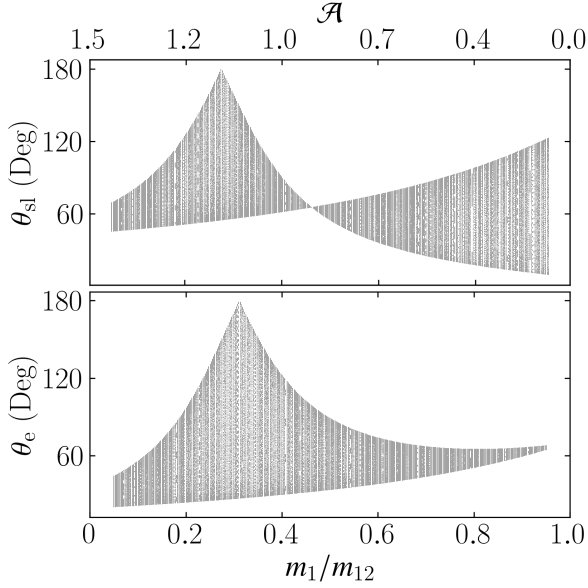
Figure 3. Bifurcation diagram for physical parameters $m_{12} = 60M_\odot$, $m_3 = 3 \times 10^7 M_\odot$, $a = 0.1$ AU, $e_0 = 10^{-3}$, $I_0 = 70°$, $a_3 = 300$ AU, and $e_3 = 0$. The initial condition is $\theta_{sl} = 0$. For each mass ratio m_1/m_{12}, the orbit-spin system is solved over 500 LK cycles, and both θ_{sl} (the angle between $\mathbf{S}$ and $\hat{\mathbf{L}}$) and θ_e [defined by Eq. (30)] are sampled at every eccentricity maximum and are plotted. The top axis shows the adiabaticity parameter $\mathscr{A}$ as defined by Eq. (35).

then evolve Eq. (25) together with the orbital evolution equations [Eqs. (4–8) without the GW terms] while sampling both θ_{sl} and θ_e at eccentricity maxima, where θ_e is given by

$$\cos\theta_e = \frac{\overline{\mathbf{\Omega}}_e}{\overline{\Omega}_e} \cdot \mathbf{S}. \tag{30}$$

We repeat this procedure with different mass ratios m_1/m_{12} of the inner binary, which only changes Ω_{SL} without changing the orbital evolution (note that the LK oscillation depends only on m_{12} and not on individual masses). Analogous to SL15, we consider systems with a range of the adibaticity parameter $\mathscr{A}$ [to be defined later in Eq. (35)] that crosses order unity. The fiducial system of Fig. 1 does not serve this purpose because the initial Ω_{SL} is too small. Our results are depicted in Fig. 3.

While our bifurcation diagram has interesting structure, the features are all regular. This is in contrast to the star-planet system studied by SL15 (see their Fig. 1). A key difference is that in our system, Ω_{SL} does not depend on θ_{sl}, while for the planet-star system, $\Omega_{SL}^{(\text{Newtonian})}$ does, and this latter feature introduces nonlinearity to the dynamics.

A more formal understanding of the dynamical behavior of our spin-orbit system comes from Floquet theory, as Eq. (25) is a linear system with periodic coefficients (the system stud-

ied in SL15 is nonlinear). Floquet's theorem says that when a linear system with periodic coefficients is integrated over a period, the evolution can be described by a linear transformation, the *monodromy matrix* $\tilde{\mathbf{M}}$, or

$$\mathbf{S}(t + P_{LK}) = \tilde{\mathbf{M}}\mathbf{S}(t), \tag{31}$$

where $\tilde{\mathbf{M}}$ is independent of $\mathbf{S}$.

While $\tilde{\mathbf{M}}$ can be easily defined, it cannot be evaluated in closed form. Thankfully, it suffices to reason directly about the properties of $\tilde{\mathbf{M}}$. In our problem, $\tilde{\mathbf{M}}$ must be a proper orthogonal matrix, or a rotation matrix, as it represents the effect of many infinitesimal rotations, each about the instantaneous $\mathbf{\Omega}_e$ [1]. Therefore, every P_{LK}, the dynamics of Eq. (25) are equivalent to a rotation about a fixed axis, prohibiting chaotic behavior.

Another traditional indicator of chaos is a positive Lyapunov exponent, obtained when the separation between nearby trajectories diverges *exponentially* in time. In Floquet theory, the Lyapunov exponent is the logarithm of the largest eigenvalue of the monodromy matrix. Since $\tilde{\mathbf{M}}$ is a rotation matrix here, the Lyapunov exponent must be 0, indicating no chaos. Numerically, we were able to verify the separation between nearby trajectories does not grow in time.

3.2. *Spin Dynamics With GW Dissipation*

When t_{GW} is finite, the coefficients $\mathbf{\Omega}_{eN}$, including $\overline{\mathbf{\Omega}}_e = \mathbf{\Omega}_{e0}$ [see Eq. (28)], are no lomg constant, but change over time. For "smooth" mergers (satisfying $t_{GW}(e_{max}) \gg t_{LK}j(e_{max})$; see Section 2), the binary goes through a sequence of LK cycles, and the coefficents vary on the LK-averaged orbital decay time $t_G W(e_{max})/j(e_{max})$. As the LK oscillation freezes, we have $\mathbf{\Omega}_e \simeq \overline{\mathbf{\Omega}}_e$ ($\mathbf{\Omega}_{eN} \simeq 0$ for $N \geq 1$), which evolves on timesale $t_{GW}(e)$ as the orbit decays and circularizes.

Once a is sufficiently small that $\Omega_{SL} \gg \Omega_L$ (this also gives $\epsilon_{GR} \gg 1$, implying the LK cycles are suppressed), it can be seen from Eq. (25) that $\theta_e = \theta_{sl}$ is constant (see bottom right panel of Fig. 1). For the fiducial parameters, we stop the simulation at $a \leq 0.5$ AU, as θ_{sl} has converged to its final value.

3.3. *Spin Dynamics Equation in Component Form*

For later analysis, it is also useful to write Eq. (28) in component form. To do so, we define inclination angle $\bar{I}_e$ as the angle between $\overline{\mathbf{\Omega}}_e$ and $\mathbf{L}_3$ as shown in Fig. 4. To express $\bar{I}_e$ algebraically, we first define LK-averaged quantities

---

[1] More formally, $\tilde{\mathbf{M}} = \tilde{\mathbf{\Phi}}(P_{LK})$ where $\tilde{\mathbf{\Phi}}(t)$ is the *principal fundamental matrix solution*: the columns of $\tilde{\mathbf{\Phi}}$ are solutions to Eq. (25) and $\tilde{\mathbf{\Phi}}(0)$ is the identity. By linearity, the columns of $\tilde{\mathbf{\Phi}}(t)$ remain orthonormal, while its determinant does not change, so $\tilde{\mathbf{M}}$ is a proper orthogonal matrix, or a rotation matrix.
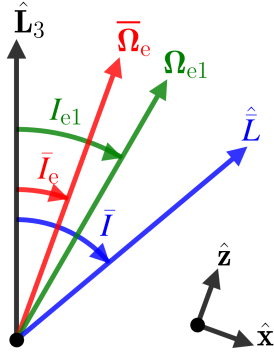
Figure 4. Definition of angles in the problem, shown in plane of the two angular momenta $\mathbf{L}_3$ and $\mathbf{L}$. Note that for $I_0 > 90°$ (and $\bar{I} > 90°$), we have $\bar{I}_e < 0$ since $\Omega_L < 0$. The bottom right shows our choice of coordinate axes.

$$\overline{\Omega_{SL} \sin I} \equiv \overline{\Omega}_{SL} \sin \bar{I}, \tag{32}$$

$$\overline{\Omega_{SL} \cos I} \equiv \overline{\Omega}_{SL} \cos \bar{I}. \tag{33}$$

It then follows that

$$\tan \bar{I}_e = \frac{\mathcal{A} \sin \bar{I}}{1 + \mathcal{A} \cos \bar{I}}, \tag{34}$$

where $\mathcal{A}$ is the adiabaticity parameter, given by

$$\mathcal{A} \equiv \frac{\overline{\Omega}_{SL}}{\overline{\Omega}_L}. \tag{35}$$

We now can choose non-inertial coordinate system where $\hat{\mathbf{z}} \propto \overline{\mathbf{\Omega}}_e$ and $\hat{\mathbf{x}}$ lies in the plane of $\mathbf{L}_3$ and $\mathbf{L}$ with positive component along $\bar{\mathbf{L}}$ (see Fig. 4). In this reference frame, the polar coordinate is just $\bar{\theta}_e$ as defined above in Eq. (40), and the equation of motion becomes

$$\frac{d\mathbf{S}}{dt} = \left[\overline{\Omega}_e \hat{\mathbf{z}} + \sum_{N=1}^{\infty} \mathbf{\Omega}_{eN} \cos\left(N\Omega_{LK}t\right) \right] \times \mathbf{S} - \dot{\bar{I}}_e \hat{\mathbf{y}} \times \mathbf{S}. \tag{36}$$

One further simplification lets us cast this vector equation of motion into a scalar form. Break $\mathbf{S}$ into components $\mathbf{S} = S_x \hat{\mathbf{x}} + S_y \hat{\mathbf{y}} + \cos \bar{\theta}_e \hat{\mathbf{z}}$ and define complex variable

$$S_{\perp} \equiv S_x + iS_y. \tag{37}$$

Then, we can rewrite Eq. (36) as

$$\frac{dS_{\perp}}{dt} = i\overline{\Omega}_e S_{\perp} - \dot{\bar{I}}_e \cos \bar{\theta}_e + \sum_{N=1}^{\infty} \Big[\cos\left(\Delta I_{eN}\right) S_{\perp}$$
$$- i \cos \bar{\theta}_e \sin\left(\Delta I_{eN}\right) \Big] \Omega_{eN} \cos\left(N\Omega_{LK}t\right). \tag{38}$$

Here, for each $\mathbf{\Omega}_{eN}$ Fourier harmonic, we denote its magnitude Ω_{eN} and its inclination angle relative to $\mathbf{L}_3$ as I_{eN} as shown in Fig. 4, and $\Delta I_{eN} = I_{eN} - \bar{I}_e$.

4. ANALYSIS: DEVIATION FROM ADIABATICITY

In general, Eq. (28) is difficult to study analytically. In this section, we neglect the hamonic terms and focus on how the varying $\overline{\mathbf{\Omega}}_e$ affects the evolution of the spin axis. The effect of the harmonic terms is studied in Section 5.

4.1. *The Adiabatic Invariant*

When neglecting the $N \geq 1$ harmonic terms, the equation of motion is modified to

$$\left(\frac{d\overline{\mathbf{S}}}{dt}\right)_{rot} = \overline{\mathbf{\Omega}}_e \times \overline{\mathbf{S}}. \tag{39}$$

It is not obvious to what extent the analysis of Eq. (39) is applicable to Eq. (28). From our numerical simulations, we find that the LK-average of $\mathbf{S}$ often evolves following Eq. (39), motivating our notation $\overline{\mathbf{S}}$. Over timescales shorter than the LK period P_{LK}, Eq. (39) loses accuracy as the evolution of $\mathbf{S}$ itself is dominated by the $N \geq 1$ harmonics we have neglected. An intuitive interpretation of this result is that the $N \geq 1$ harmonics vanish when integrating Eq. (28) over a LK cycle.

Eq. (39) has one desirable property: $\bar{\theta}_e$, given by

$$\cos \bar{\theta}_e \equiv \overline{\mathbf{S}} \cdot \frac{\overline{\mathbf{\Omega}}_e}{\overline{\Omega}_e}, \tag{40}$$

is an adiabatic invariant. The adiabaticity condition requires the precession axis evolve slowly compared to the precession frequency at all times, i.e.

$$\left| \frac{d\bar{I}_e}{dt} \right| \ll \overline{\Omega}_e. \tag{41}$$

For the simulation shown in Fig. 1, the values of $\dot{\bar{I}}_e$ and $\overline{\Omega}_e$ are shown in the top panel of Fig. 5, and the evolution of $\bar{\theta}_e$ in the bottom panel. Since $\left| \dot{\bar{I}}_e \right| \ll \left| \overline{\Omega}_e \right|$ at all times, and the total change in $\bar{\theta}_e$ in this simulation is $0.01°$, small as expected.

4.2. *Calculating Deviation from Adiabaticity*

In real systems, the extent to which $\bar{\theta}_e$ is conserved depends on how well Eq. (41) is satisfied. In this subsection, we derive a bound on the total non-conservation of $\bar{\theta}_e$, then in the next subsection we show this bound can be estimated from initial conditions.

When neglecting harmonic terms, the scalar equation of motion Eq. (38) becomes

$$\frac{dS_{\perp}}{dt} = i\overline{\Omega}_e S_{\perp} - \dot{\bar{I}}_e \cos \bar{\theta}_e. \tag{42}$$

This can be solved in closed form. Defining

$$\Phi(t) \equiv \int^t \overline{\Omega}_e \, dt, \tag{43}$$

we obtain the solution between the initial time t_i and the final time t_f:

$$e^{-i\Phi} S_\perp \Big|_{t_i}^{t_f} = -\int_{t_i}^{t_f} e^{-i\Phi(\tau)} \dot{\bar{I}}_e \cos \bar\theta_e \, d\tau. \qquad (44)$$

Recalling $|S_\perp| = \sin \bar\theta_e$ and analyzing Eq. (44), we see that $\bar\theta_e$ oscillates about its initial value with amplitude

$$\left| \Delta \bar\theta_e \right| \sim \left| \frac{\dot{\bar{I}}_e}{\bar\Omega_e} \right|. \qquad (45)$$

We see that in the adiabatic limit [Eq. (41)], $\bar\theta_e$ is indeed conserved, as the right hand side goes to zero. The bottom panel of Fig. 5 shows $\Delta\bar\theta_e$ for the fiducial simulation. Note that $\bar\theta_e$ is indeed mostly constant where Eq. (45) predicts small oscillations.

If we denote $\left| \Delta \bar\theta_e \right|^f$ to be the total change in $\bar\theta_e$ over $t \in [t_i, t_f]$, we can give a loose bound

$$\left| \Delta \bar\theta_e \right|^f \lesssim \left| \frac{\dot{\bar{I}}_e}{\bar\Omega_e} \right|_{\max}. \qquad (46)$$

Inspection of Fig. 5 indicates that the spin dynamics are mostly uninteresting except near the peak of $\dot{\bar{I}}_e$, which occurs when where $\Omega_{SL} \simeq |\Omega_L|$. We present a zoomed-in view of the behavior of all dynamical quantities near the peak of $\dot{\bar{I}}_e$ in the fiducial simulation in Fig. 6. In particular, in the bottom-rightmost panel, we see that the fluctuations in $\bar\theta_e$ are dominated by a second contribution, the subject of the discussion in Section 5.

For comparison, we show in Fig. 7 a more rapid binary merger starting with $I_0 = 90.2°$, for which $|\Delta\theta_e|^f \approx 2°$. If we again examine the bottom-rightmost plot, we see that the fluctuations in $\Delta\bar\theta_e$ are well described by Eq. (45).

4.3. *Estimate of Deviation from Adiabaticity from Initial Conditions*

To estimate $\left| \dot{\bar{I}}_e / \bar\Omega_e \right|_{\max}$ from initial conditions, we first differentiate Eq. (34),
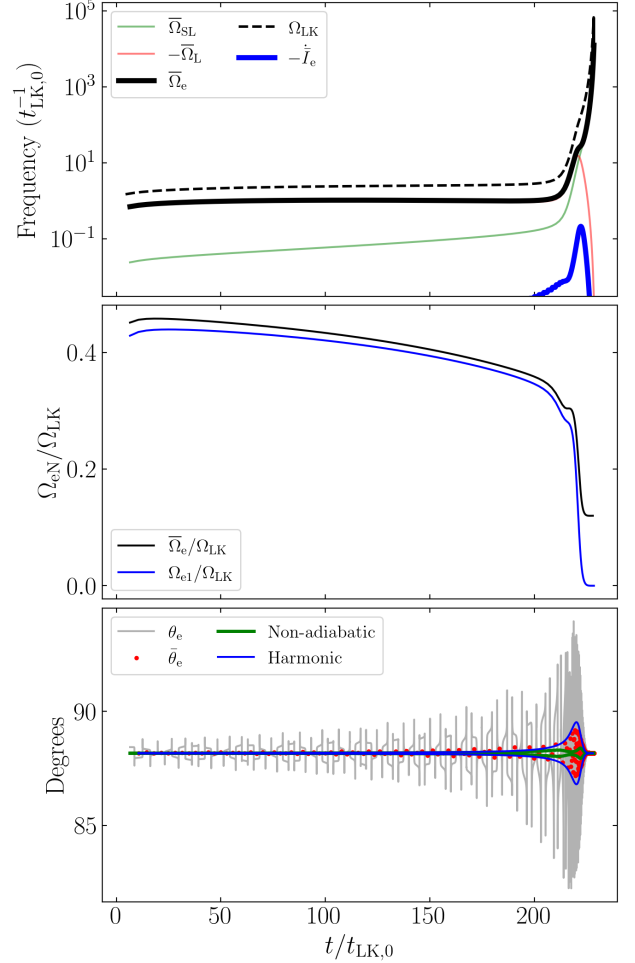
$$\dot{\bar{I}}_e = \left(\frac{\dot{\mathcal{A}}}{\mathcal{A}} \right) \frac{\mathcal{A} \sin \bar{I}}{1 + 2\mathcal{A} \cos \bar{I} + \mathcal{A}^2}. \qquad (47)$$

It also follows from Eq. (26) that

$$\overline{\Omega}_e = \overline{\Omega}_L \left(1 + 2\mathcal{A} \cos \bar{I} + \mathcal{A}^2 \right)^{1/2}, \qquad (48)$$

from which we obtain

$$\left| \frac{\dot{\bar{I}}_e}{\overline{\Omega}_e} \right| = \left(\frac{\dot{\mathcal{A}}}{\mathcal{A}} \right) \frac{1}{|\overline{\Omega}_L|} \frac{\mathcal{A} \sin \bar{I}}{\left(1 + 2\mathcal{A} \cos \bar{I} + \mathcal{A}^2 \right)^{3/2}}. \qquad (49)$$

Figure 5. The same simulation as depicted in Fig. 1 but showing the calculated quantities relevant to the theory of the paper over the entire course of the simulation. Top: the important frequencies of the system. Middle: the frequency ratios between the zeroth and first Fourier components of $\mathbf{\Omega}_e$ to the LK frequency Ω_{LK}. Bottom: Plot of θ_e [grey line; Eq. (30)], $\bar\theta_e$ [red dots; Eq. (40)], as well as estimates of the deviations from perfect conservation of $\bar\theta_e$ due to non-adiabaticity [green, Eq. (45)] and due to resonances with harmonic terms [blue, Eq. (68)].
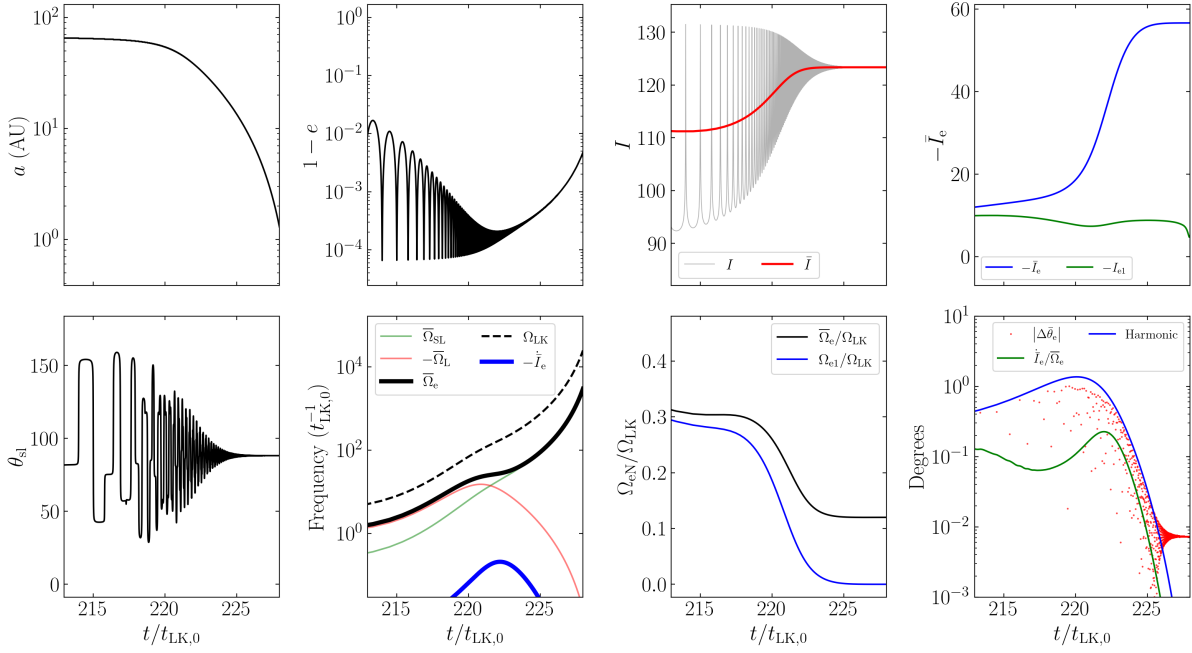
Moreover, if we assume the eccentricity is frozen around $e \simeq 1$ and $\cos^2 \omega \simeq 1/2$ in $d\Omega/dt$, we obtain the estimate

$$\mathcal{A} \simeq \frac{3Gn(m_2 + \mu/3)}{2c^2 a j^2} \left[\frac{15 \cos \bar{I}}{8 t_{LK} j} \right]^{-1}, \qquad (50)$$

$$\simeq \frac{4}{5} \frac{G(m_2 + \mu/3) m_{12} \tilde{a}_3^3}{c^2 m_3 a^4 j \cos \bar{I}}, \qquad$$

$$\frac{\dot{\mathcal{A}}}{\mathcal{A}} = -4 \left(\frac{\dot{a}}{a} \right)_{GW} + \frac{e}{j^2} \left(\frac{de}{dt} \right)_{GW}. \qquad (51)$$

$$(52)$$

Figure 6. The same simulation as Fig. 1 but zoomed in on the region around $\mathcal{A} \equiv \overline{\Omega}_{\rm SL}/\left|\overline{\Omega}_{\rm L}\right| \simeq 1$. The first three panels in the upper row depict a, e, I and $\bar{I}$ as in Fig. 1, while the fourth shows $I_{\rm e}$ [Eq. (34)] and $I_{\rm e1}$. The bottom four panels depict $\theta_{\rm sl}$, the five characteristic frequencies of the system [Eqs. 26 and (27)] (as in the top panel of Fig. 5), the relevant frequency ratios (as in the middle panel of Fig. 5), and the deviation of $\bar{\theta}_{\rm e}$ from its initial value compared to the predictions of Eqs. (45) and (68).
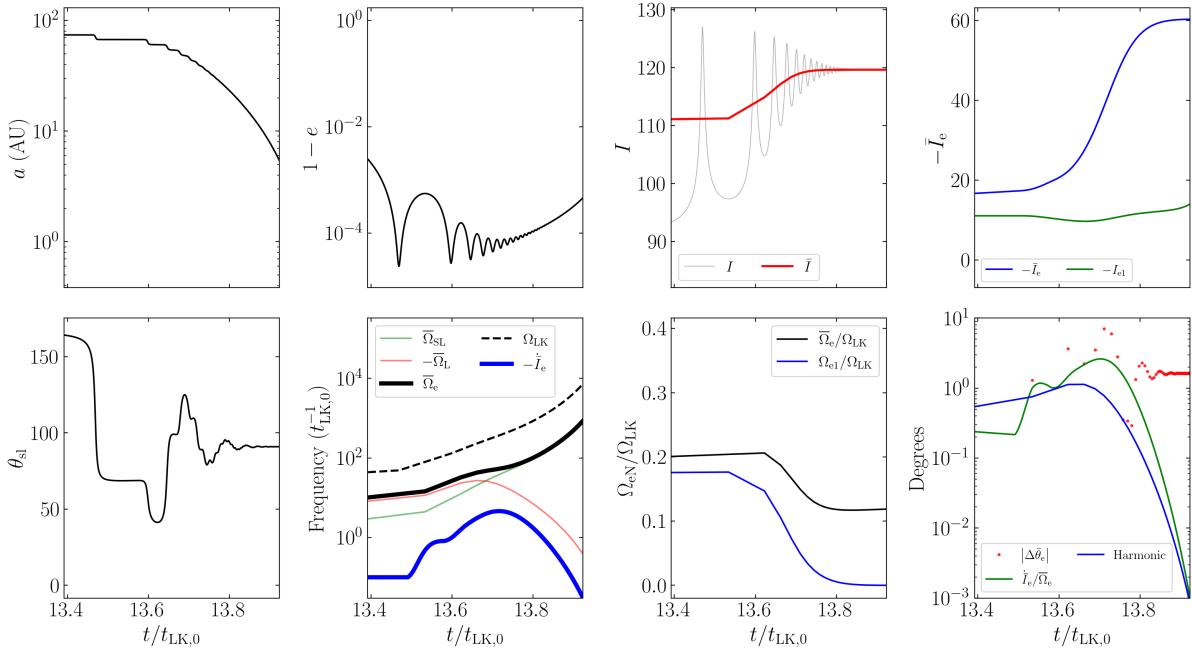
Figure 7. Same as Fig. 6 except for $I_0 = 90.2°$, corresponding to a faster coalescence. The total change in $\bar{\theta}_{\rm e}$ for this simulation is $\approx 2°$.

With these, we see that Eq. (49) is small except when $\mathcal{A} \simeq 1$, and so we find that the maximum $\left| \dot{\bar{I}}_e / \overline{\Omega}_e \right|$ is given roughly by

$$\left| \frac{\dot{\bar{I}}_e}{\overline{\Omega}_e} \right|_{\max} \simeq \left(\frac{\dot{\mathcal{A}}}{\mathcal{A}} \right) \frac{1}{\left| \overline{\Omega}_L \right|} \frac{\sin \bar{I}}{(2 + 2 \cos \bar{I})^{3/2}}. \tag{53}$$

To evaluate this, we make two assumptions: (i) $\bar{I}$ is approximately constant (see third panels of Figs. 6 and 7), and (ii) $j(e)$ evaluated at $\mathcal{A} \simeq 1$ can be approximated as a constant multiple of the initial $j(e_{\max})$, so that

$$j_\star \equiv j(e_\star) = f \sqrt{\frac{5}{3} \cos^2 I_0}, \tag{54}$$

where star subscripts denote evaluation at $\mathcal{A} \simeq 1$, for some unknown factor $f > 1$. f turns out to be relatively insensitive to I_0. This reflects the fact that systems with lower $e_{\max}$ values take more cycles to attain $\mathcal{A} \simeq 1$, so all systems experience a similar amount of decay due to GW radiation.

For simplicity, let's first assume $\mathcal{A} \simeq 1$ is satisfied when the LK oscillations are mostly suppressed, and $e_\star \approx 1$ is a constant throughout the LK cycle (see second panels of Figs. 6 and 7; we will later see that the scalings are the same in the LK-oscillating regime). Approximating $e_\star \approx 1$ in Eqs. (14) and (13) gives

$$\left[\frac{\dot{\mathcal{A}}}{\mathcal{A}} \right]_\star \simeq \frac{G^3 \mu m_{12}^2}{c^5 a_\star^4 j_\star^7} \frac{595}{3}. \tag{55}$$

To fix $a_\star$, we require Eq. (51) to give $\mathcal{A} = 1$ for $a_\star$ and $j_\star$. Taking all of these together, we obtain

$$\left| \frac{\dot{\bar{I}}_e}{\overline{\Omega}_e} \right|_{\max} \approx \frac{595 \sin(\bar{I}) \left| \cos(\bar{I}) \right|^{3/8}}{36 j^{\frac{37}{8}} \left(\cos(\bar{I}) + 1 \right)^{\frac{3}{2}}} \left(\frac{8000 G^9 m_{12}^9 m_3^3 \mu^8}{\tilde{a}_3^9 c^{18} (m_2 + \mu/3)^{11}} \right)^{1/8}. \tag{56}$$

We can also calculate $\dot{\bar{I}}_e / \overline{\Omega}_e$ from numerical simulations. Taking characteristic $\bar{I} \approx 120°$ (Figs. 6 and 7 show that this is a serviceable approximation that holds across a range of I_0), we can fit the last remaining free parameter f [Eq. (54)] to the data from numerical simulations. This yields $f \approx 2.72$, leading to final result

$$\left| \frac{\dot{\bar{I}}_e}{\overline{\Omega}_e} \right|_{\max} = 0.98° \left(\frac{\cos I_0}{\cos(90.3°)} \right)^{-37/8} \left(\frac{\tilde{a}_3}{2.2 \text{ pc}} \right)^{-9/8}$$

$$\times \left(\frac{m_3}{3 \times 10^7 \, M_\odot} \right)^{3/8}. \tag{57}$$

The result of this fit is shown in Fig. 8, where it is clear the scaling predicted by Eq. (57) is remarkably accurate.

Above, we assumed that the system evolves through $\mathcal{A} \simeq 1$ when the eccentricity is mostly frozen (see Fig. 1 for an indication of how accurate this is for the parameter space explored in Fig. 8). It is also possible that $\mathcal{A} \simeq 1$ occurs when
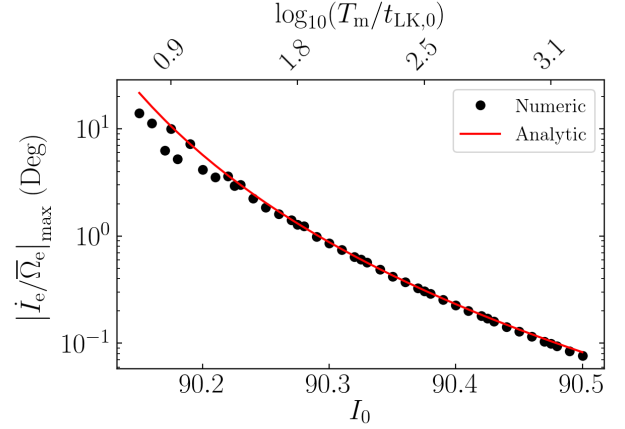
Figure 8. Comparison of $\left| \dot{\bar{I}}_e / \overline{\Omega}_e \right|_{\max}$ extracted from simulations and using Eq. (57), where we take $f = 2.72$ in Eq. (54). The coalescence time T_m is shown along the top axis of the plot in units of the characteristic LK timescale at the start of inspiral $t_{\mathrm{LK},0}$; the LK period is initially of order a few $t_{\mathrm{LK},0}$. The agreement is remarkable for systems that coalesce over many $t_{\mathrm{LK},0}$.

the eccentricity is still undergoing substantial oscillations. In fact, Eq. (57) is still accurate in this regime when replacing e with $e_{\max}$, due to the following analysis. Recall that when $e_{\min} \ll e_{\max}$, the binary spends a fraction $\sim j(e_{\max})$ of the LK cycle near $e \simeq e_{\max}$ (Anderson et al. 2016). This fraction of the LK cycle dominates both GW dissipation and $\overline{\Omega}_e$ precession. Thus, both $\dot{\bar{I}}_e$ and $\overline{\Omega}_e$ in the oscillating-e regime are evaluated by setting $e \approx e_{\max}$ and adding a prefactor of $j(e_{\max})$. The prefactors of $j(e_{\max})$ cancel when computing the quotient $\dot{\bar{I}}_e / \overline{\Omega}_e$.

The accuracy of Eq. (57) in bounding $\left| \Delta \bar{\theta}_e \right|^f$ is shown in Fig. 9. Note that conservation of $\bar{\theta}_e$ is generally much better than Eq. (57) predicts. This is because cancellation of phases in Eq. (44) is generally more efficient than Eq. (57) assumes.

4.4. θ_{sl}^f Behavior

In Fig. 2, we show θ_{sl}^f as a function of I_0 when $\theta_{\mathrm{sl}}^i = 0$. With the results developed in the previous sections, we can understand the behavior seen in this plot.

First, while $\bar{\theta}_e$ is our proposed adiabatic invariant, $\bar{\theta}_e^i$ is not measurable. As such, we re-express $\bar{\theta}_e$ in terms of physical quantities. We work in the inertial frame of reference and choose spherical coordinate system where $\mathbf{L}_3 \propto \hat{\mathbf{Z}}$. We then specify $\mathbf{S}$ by the polar and azimuthal angles θ_{s3} and ϕ_{s3} respectively. We follow the same convention as before and choose $\hat{\mathbf{X}}$ to point along $\hat{\mathbf{L}}$. Finally, we will consider the case of nonzero $\eta \equiv L/L_3$ here, to better parallel the discussion in LL18. In this case, $\overline{\boldsymbol{\Omega}}_e$ is given by (Liu & Lai 2017)

$$\overline{\boldsymbol{\Omega}}_e = \overline{\Omega}_{\mathrm{SL}} \hat{\mathbf{L}} + \overline{\Omega}_L \frac{\mathbf{L}_{\mathrm{tot}}}{L_3}, \tag{58}$$
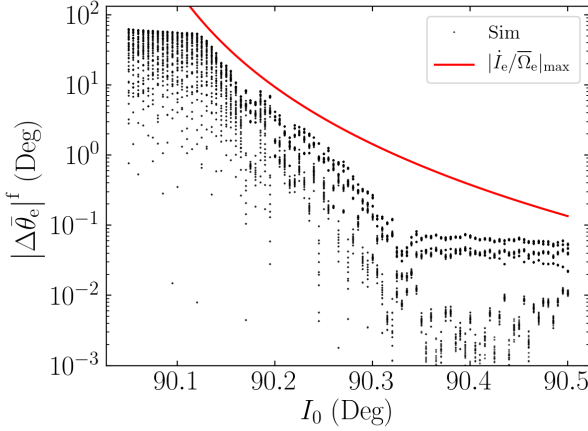
Figure 9. Total change in $\bar{\theta}_e$ over inspiral as a function of initial inclination I_0, where the initial $\overline{\Omega}_e$ is computed without GW dissipation. For each I_0, 100 simulations are run for **S** on a uniform, isotropic grid. Plotted for comparison is the bound $\left|\Delta\bar{\theta}_e\right|^f \lesssim \left|\dot{I}_e/\overline{\Omega}_e\right|_{\max}$, using the analytical scaling given by Eq. (57). It is clear that the given bound is not tight but provides an upper bound for non-conservation of $\bar{\theta}_e$ due to nonadiabatic effects. At the right of the plot, the accuracy saturates: this is because neglecting GW dissipation causes inaccuracies when computing the average $\overline{\Omega}_e$.

where

$$\mathbf{L}_{\text{tot}} \equiv \mathbf{L} + \mathbf{L}_3. \tag{59}$$

It can then be shown that

$$\overline{\mathbf{\Omega}}_e = \overline{\Omega}_L \left[(\mathcal{A} + \eta) \sin \bar{I} \, \hat{\mathbf{X}} + \left(\mathcal{A} \cos \bar{I} + \eta \cos \bar{I} + 1 \right) \hat{\mathbf{Z}} \right]. \tag{60}$$

Then, for some $\mathbf{S} = \cos\theta_{s3}\hat{\mathbf{Z}} + \sin\theta_{s3}\left(\cos\phi_{s3}\hat{\mathbf{X}} + \sin\phi_{s3}\hat{\mathbf{Y}}\right)$, we can calculate

$$\cos\bar{\theta}_e = \frac{(\mathcal{A} + \eta)\,\theta_{sl} \pm \cos\theta_{s3}}{\sqrt{(\mathcal{A} + \eta)^2 \pm 2(\mathcal{A} + \eta)\cos I + 1}}. \tag{61}$$

The sign in the above equation is equal to $\text{sgn}\left(\overline{\Omega}_L\right)$, i.e. positive for $I_0 < 90°$ and negative for $I_0 > 90°$. We remark that our equation is a generalization of Eq. (73) of LL18, where they assume $e = 0$, $\bar{I} = I$, and $\mathbf{S}_i = \hat{\mathbf{L}}$ (initial spin-orbit alignment). This implies $\theta_{s3} = I$ while $\phi_{s3} = 0$ as well, and Eq. (61) simplifies and agrees with LL18 [when $e = 0$, their $\mathcal{A}_0/2 \cos I_0$ is our $\mathcal{A}$; see their Eq. (72)].

Note that, for the fiducial parameter space, $\mathcal{A} \ll 1$ initially (Fig. 5), and $\eta \ll 1$ as well, so Eq. (61) simply gives

$$\bar{\theta}_e^i \approx \begin{cases} \theta_{sb}^i & I_0 < 90°, \\ 180° - \theta_{sb}^i & I_0 > 90°, \end{cases} \tag{62}$$

On the other hand, at late times, $\mathcal{A} \gg 1$, and $\bar{\theta}_e^f = \theta_{sl}^f$. Thus, when $\bar{\theta}_e$ is conserved, we obtain

$$\theta_{sl}^f \approx \begin{cases} \theta_{sb}^i & I_0 < 90°, \\ 180° - \theta_{sb}^i & I_0 > 90°, \end{cases} \tag{63}$$

This shows that we expect $\theta_{sl}^f \in [89.5°, 90°]$ for mergers in Fig. 2 sufficiently far from $I_0 = 90°$, which is indeed observed. This is the origin of the 90° attractor. This is further in agreement with the recent results in Yu et al. (2020), where they studied arbitrary initial $\mathbf{S}_i$ orientations and obtained exactly Eq. (63) [see their Eq. (46), bottom panel of Fig. 4].

Above, we have analyzed the θ_{sl}^f distribution for smooth mergers. Next, we can consider rapid mergers, for which $\bar{\theta}_e$ conservation is imperfect. Earlier, we showed this non-conservation obeys Eq. (57), and so we expect

$$\left|\theta_{sl}^f - \bar{\theta}_e^i\right| \lesssim \left|\Delta\bar{\theta}_e\right|^f. \tag{64}$$

This is overplotted as the black dotted line in Fig. 2, and we see it mostly captures the deviation of θ_{sl}^f from $\sim 90°$ except very near $I_0 = 90°$. This is expected, as Eq. (57) is singular for $I_0 = 90°$, and it is expected to lose accuracy in this regime as shown in Fig. 9.

When $I_0 = 90°$ exactly, we can show that $\theta_{sl}^f = \theta_{sl}^i$: when $I_0 = 90°$, $dI/dt = 0$ by Eq. (7), so $I = 90°$ for all time. Then, $d\Omega/dt = 0$ for $I = 90°$ [Eq. (6)], implying that **L** is constant. Thus, **S** precesses around a constant vector, and the opening angle can never change. In Fig. 2, $\theta_{sl}^i = 0$, so indeed we find $\theta_{sl}^f = 0$.

Finally, Fig. 2 shows that the true θ_{sl}^f are oscillatory within the envelope bounded by Eq. (64) above. This can also be understood: Eq. (46) only bounds the maximum of the absolute value of the change in $\bar{\theta}_e$, while the actual change depends on the initial and final complex phases of $S_\perp$ in Eq. (44), denoted $\Phi(t_i)$ and $\Phi(t_f)$. When $\theta_{sl}^i = 0$, we have $\Phi(t_i) = 0$, as **S** starts in the $\hat{\mathbf{x}}$-$\hat{\mathbf{z}}$ plane. Then, as I_0 is smoothly varied, the final phase $\Phi(t_f)$ must also vary smoothly [since $\overline{\Omega}_e$ in Eq. (43) is a continuous function, $\Phi(t)$ must be as well], so the total phase difference between the initial and final values of $S_\perp$ varies smoothly. This means the total change in $\bar{\theta}_e$ will fluctuate smoothly between $\pm\left|\Delta\bar{\theta}_e\right|^f$ as I_0 is changed, giving rise to the sinusoidal shape seen in Fig. 2.

5. ANALYSIS: EFFECT OF RESONANCES

In the previous section, we neglected the $N \geq 1$ Fourier harmonics in Eq. (28), and showed that the final θ_{sl}^f behavior could be completely explained. In this section, we study one effect of the Fourier harmonics that occurs when two frequencies become commensurate. We show this effect can be neglected for the fiducial parameter regime. A regime for which the Fourier harmonics cannot be neglected is discussed separately in Section 6.

For simplicity, we ignore the effects of GW dissipation in this section and assume the system is exactly periodic (so $\dot{I}_e = 0$). The scalar equation of motion Eq. (38) is then:

$$\frac{dS_\perp}{dt} = i\overline{\Omega}_e S_\perp + \sum_{N=1}^{\infty} [\cos(\Delta I_{eN}) S_\perp$$
$$- i\cos\theta\sin(\Delta I_{eN})]\Omega_{eN}\cos(N\Omega_{LK}t). \quad (65)$$

Resonances can occur when $\overline{\Omega}_e = N\Omega_{LK}$. Numerically, we find that $\overline{\Omega}_e \lesssim \Omega_{LK}$ for most regions of parameter space (see Fig. 10, and recall that LK-induced mergers only complete within a Hubble time when $I_{min} \approx 90°$). Accordingly, we restrict our analysis to resonances with the $N = 1$ component. For simplicity, we also ignore the modulation of the forcing frequency in Eq. (65). While this fails to capture the possibility of a parametric resonance, we find no evidence for parametric resonances in our simulations. With these two simplifications, Eq. (65) further reduces to

$$\frac{dS_\perp}{dt} \approx i\overline{\Omega}_e S_\perp - i\cos\bar{\theta}_e\sin(\Delta I_{e1})\Omega_{e1}\cos(\Omega_{LK}t). \quad (66)$$

We can approximate $\cos(\Omega_{LK}t) \approx e^{i\Omega_{LK}t}/2$, as the $e^{-i\Omega_{LK}t}$ component is far from resonance. Then we can write down solution as before

$$e^{-i\overline{\Omega}_e t} S_\perp \Big|_{t_i}^{t_f} = -\int_{t_i}^{t_f} \frac{i\sin(\Delta I_{e1})\Omega_{e1}}{2} e^{-i\overline{\Omega}_e t + i\Omega_{LK}t}\cos\bar{\theta}_e\, dt. \quad (67)$$

Thus, similarly to Section 4.2, the instantaneous oscillation amplitude $|\Delta\bar{\theta}_e|$ can be bound by

$$|\Delta\bar{\theta}_e| \sim \frac{1}{2}\left|\frac{\sin(\Delta I_{e1})\Omega_{e1}}{\Omega_{LK} - \overline{\Omega}_e}\right|. \quad (68)$$

We see that if $\overline{\Omega}_e < \Omega_{LK}$ by a sufficient margin for all times, then the conservation of $\bar{\theta}_e$ in the fiducial parameter regime cannot be significantly affected by this resonance. The ratio $\overline{\Omega}_e/\Omega_{LK}$ is shown in the middle panel of Fig. 5, and the amplitude of oscillation of $\bar{\theta}_e$ it generates [Eq. (68)] is given in blue in the bottom panel of Fig. 5. We see that the total effect of the harmonic terms never exceeds a few degrees.

Furthermore, we see from Fig. 6 (top rightmost panel and third panel of bottom row) that the interesting dynamics, occuring when Ω_{e1} and ΔI_{e1} are both nonzero [necessary for Eq. (68) to be nonzero], occur in the regime $\mathcal{A} \simeq 1$. Then, the bottom-rightmost panel of Fig. 6 compares the detailed behavior of $\bar{\theta}_e$ and its two contributions, the nonadiabatic and harmonic effects. We see that Eq. (68) describes the oscillations in $\bar{\theta}_e$ very well. The agreement is poorer in the bottom-rightmost panel of Fig. 7, as the nonadiabatic effect is much stronger. However, note that the theory presented in the
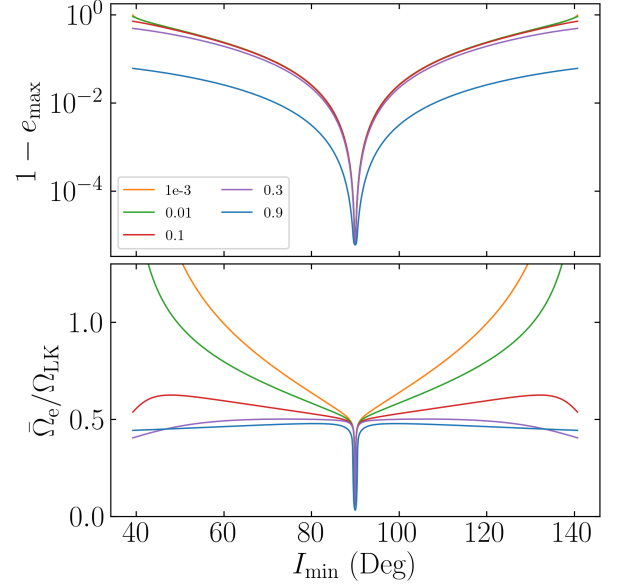
Figure 10. e_{max} and $\overline{\Omega}_e/\Omega_{LK}$ as a function of I_{min}, the inclination of the inner binary at eccentricity minimum, for varying values of e_{min} (different colors) for the fiducial parameter regime.

previous section captures the final deviations $|\Delta\bar{\theta}_e|^f$ very well (see Fig. 9 for $I_0 = 90.35°$). This suggests that oscillations in $\bar{\theta}_e$ due to harmonic perturbations of up to a few degrees do not affect final nonconservation by more than $\sim 0.01°$.

6. LIDOV-KOZAI ENHANCED MERGERS

In LL17, a different parameter regime is considered, where the inner binary is sufficiently close in (~ 0.1 AU) that it can merge in isolation via GW radiation, given by: $m_1 = m_2 = m_3 = 30M_\odot$, $a_{in} = 0.1$ AU, $\tilde{a}_3 = 3$ AU, and $e_3 = 0$. Note that m_3 here is not an SMBH. However, our results can still be applied judiciously to this parameter regime and yield interesting insights.

First, we recall the θ_{sl}^f distribution obtained via numerical simulation, shown in Fig. 11. LL17 derives an adiabatic invariant assuming the inner binary does not undergo eccentricity oscillations. Our result, based on $\bar{\theta}_e$ conservation, is a generalization of their result, giving the same result when the inner orbit remains circular. Very near $I_0 \approx 90°$, the data are offset somewhat from our result, because we have assumed the tertiary's angular momentum is fixed, but accounting for the offset, our theory captures the scaling of θ_{sl}^f, as seen in Fig. 12.

However, as can be seen in Fig. 11, intermediate inclinations $I_0 \in [50, 80]$ and $I_0 \in [100, 130]$ exhibit very volatile behavior in θ_{sl}^f. This is unlike the plots generated in the fiducial parameter regime (Fig. 2), as this inclination regime corresponds to neither the fastest nor slowest merging systems. We attribute the origin of this volatility to a stronger
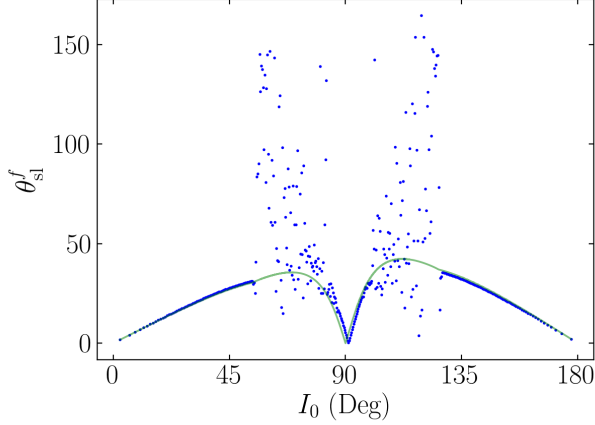
Figure 11. Plot of $\theta_{\rm sl}^{\rm f}$ for the LK-enhanced parameter regime, i.e. $m_1 = m_2 = m_3 = 30 M_\odot$, $a_{\rm in} = 0.1$ AU, $\tilde{a}_3 = 3$ AU, and $e_3 = 0$. Conservation of $\bar{\theta}_{\rm e}$ gives the green line. Agreement near $I_0 = 90°$ is good when accounting for the effects of a finite L_3 (see Fig. 12). For I_0 in the two intervals $[40°, 80°]$ and $[100°, 140°]$, a further effect causes $\theta_{\rm sl}^{\rm f}$ to fluctuate unpredictably.
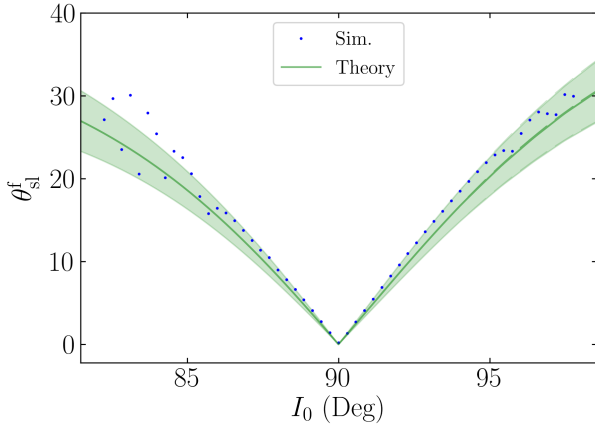
Figure 12. Zoomed in version of Fig. 11 near $I_0 \approx 90°$ while adding an I_0 offset to account for differences between the data and theory due to finite L_3 effects. The green shaded area shows the expected range of deviations due to resonant perturbations following Eq. (68) (evaluated for the initial system parameters). The data nearer 90° have less spread than predicted, but the transition to a larger $\theta_{\rm sl}^{\rm f}$ spread roughly follows the prediction of the green line.

resonant interaction. By examining Fig. 13, it is evident that, for the same $e_{\rm min}$, systems with $I_{\rm min}$ further from 90° are closer to the $\bar{\Omega}_{\rm e} = \Omega_{\rm LK}$ resonance. Outside of the LK window, $\bar{\Omega}_{\rm e}$ also goes swiftly to zero, as seen in Fig. 13, so this explanation is consistent with the ranges of inclinations that exhibit volatile $\theta_{\rm sl}^{\rm f}$ behavior. We forgo further investigation of this mechanism because it is not expected to play an impor-
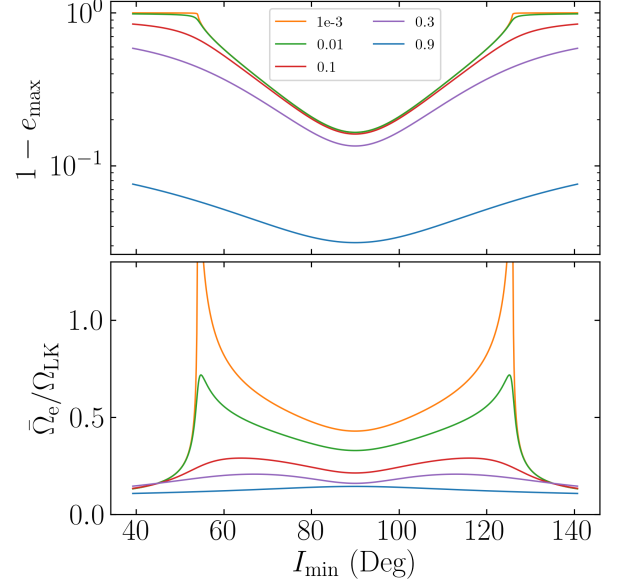
Figure 13. Same as Fig. 10 but for the compact parameter regime. Cmopared to Fig. 10, we see that $e_{\rm max}$ is smaller due to stronger pericenter precession $\Omega_{\rm GR}$ in this regime, so the $\bar{\Omega}_{\rm e}/\Omega_{\rm LK} = 1$ resonance is accessible for a wide range of parameter space. In particular, both smaller $e_{\rm min}$ and $e_{\rm max}$ values bring the system closer to the resonance.

tant role in any LK-induced BH binary mergers for reasons discussed below.

At first, it seems clear from Fig. 10 that $\bar{\Omega}_{\rm e}$ is significantly smaller than $\Omega_{\rm LK}$ near $I_{\rm min} \approx 90°$ for LK-induced mergers. However, this is not sufficient to guarantee that the frequency ratio remains small for the entire evolution, as GR effects become stronger as the binary coalesces. Instead, a more careful analysis of the relevant quantities in Eq. (68) proves useful:

- $\sin(\Delta I_{\rm e1})$ is small unless $\mathcal{A} \simeq 1$. Otherwise, $\mathbf{\Omega}_{\rm e}$ does not nutate appreciably within an LK cycle, and all the $\mathbf{\Omega}_{\rm eN}$ are aligned with $\bar{\mathbf{\Omega}}_{\rm e}$, implying all the $\Delta I_{\rm eN} \approx 0$.

- Smaller values of $e_{\rm min}$ increase $\bar{\Omega}_{\rm e}/\Omega_{\rm LK}$, as shown in Fig. 13.

However, LK-driven coalescence causes $\mathcal{A}$ to increase on a similar timescale to that of $e_{\rm min}$ increase (see Fig. 1). This implies that, if $\mathcal{A} \ll 1$ initially, which is the case for LK-induced mergers, then $e_{\rm min}$ will be very close to 1 when $\mathcal{A}$ grows to be $\simeq 1$, and the contribution predicted by Eq. (68) must be small.

7. CONCLUSION AND DISCUSSION

In this paper, we consider the evolution of the spin-orbit misalignment angle $\theta_{\rm sl}$ of a black hole (BH) binary that merges under gravitational wave (GW) radiation during

Lidov-Kozai (LK) oscillations induced by a tertiary supermassive black hole (SMBH). We show that, when the gravitational potential of the SMBH is handled at quadrupolar order, the spin vectors of the inner BHs obey the simple equation of motion Eq. (25). Analysis of this equation yields the following conclusions:

- Since Eq. (25) is a linear system with periodically varying coefficients, it cannot give rise to chaotic dynamics by Floquet's Theorem.

- For most parameters of astrophysical relevance, the angle $\bar{\theta}_e$ [Eq. (40)] is an adiabatic invariant. Since the inner BH binary merges in finite time, $\bar{\theta}_e$ is only conserved to finite accuracy; we show that the deviation from perfect adiabaticity can be predicted from initial conditions.

- When the resonant condition $\bar{\Omega}_e \approx \Omega_{LK}$ is satisfied, significant oscillations in $\bar{\theta}_e$ can arise. We derive an analytic estimate of this oscillation amplitude. This estimate both demonstrates that the resonance is unimportant for "LK-induced" mergers and tentatively explains the scatter in θ_{sl}^f seen by LL17.

REFERENCES

Abbott, B., et al. 2016, Phys. Rev. Lett., 116, 061102, doi: 10.1103/PhysRevLett.116.061102

Abbott, B., Abbott, R., Abbott, T., et al. 2019, The Astrophysical Journal Letters, 882, L24

Anderson, K. R., Storch, N. I., & Lai, D. 2016, Monthly Notices of the Royal Astronomical Society, 456, 3671

Antonini, F., & Perets, H. B. 2012, The Astrophysical Journal, 757, 27

Antonini, F., Toonen, S., & Hamers, A. S. 2017, The Astrophysical Journal, 841, 77

Banerjee, S., Baumgardt, H., & Kroupa, P. 2010, Monthly Notices of the Royal Astronomical Society, 402, 371

Belczynski, K., Dominik, M., Bulik, T., et al. 2010, The Astrophysical Journal Letters, 715, L138

Belczynski, K., Holz, D. E., Bulik, T., & O'Shaughnessy, R. 2016, Nature, 534, 512

Belczynski, K., Klencki, J., Fields, C., et al. 2020, Astronomy & Astrophysics, 636, A104

Blaes, O., Lee, M. H., & Socrates, A. 2002, The Astrophysical Journal, 578, 775

Dominik, M., Belczynski, K., Fryer, C., et al. 2012, The Astrophysical Journal, 759, 52

—. 2013, The Astrophysical Journal, 779, 72

Dominik, M., Berti, E., O'Shaughnessy, R., et al. 2015, The Astrophysical Journal, 806, 263

Downing, J., Benacquista, M., Giersz, M., & Spurzem, R. 2010, Monthly Notices of the Royal Astronomical Society, 407, 1946

Gondán, L., Kocsis, B., Raffai, P., & Frei, Z. 2018, The Astrophysical Journal, 860, 5

Hoang, B.-M., Naoz, S., Kocsis, B., Rasio, F. A., & Dosopoulou, F. 2018, The Astrophysical Journal, 856, 140

Kinoshita, H. 1993, Celestial Mechanics and Dynamical Astronomy, 57, 359

Kozai, Y. 1962, The Astronomical Journal, 67, 591

Lidov, M. L. 1962, Planetary and Space Science, 9, 719

Lipunov, V., Postnov, K., & Prokhorov, M. 1997, Astronomy Letters, 23, 492

Lipunov, V., Kornilov, V., Gorbovskoy, E., et al. 2017, Monthly Notices of the Royal Astronomical Society, 465, 3656

Liu, B., & Lai, D. 2017, The Astrophysical Journal Letters, 846, L11

—. 2018, The Astrophysical Journal, 863, 68

Liu, B., Lai, D., & Wang, Y.-H. 2019, The Astrophysical Journal, 881, 41

Miller, M. C., & Hamilton, D. P. 2002, The Astrophysical Journal, 576, 894

Miller, M. C., & Lauburg, V. M. 2009, The Astrophysical Journal, 692, 917

O'leary, R. M., Rasio, F. A., Fregeau, J. M., Ivanova, N., & O'Shaughnessy, R. 2006, The Astrophysical Journal, 637, 937

Peters, P. C. 1964, Physical Review, 136, B1224

Podsiadlowski, P., Rappaport, S., & Han, Z. 2003, Monthly Notices of the Royal Astronomical Society, 341, 385

Postnov, K., & Kuranov, A. 2019, Monthly Notices of the Royal Astronomical Society, 483, 3288

Randall, L., & Xianyu, Z.-Z. 2018, The Astrophysical Journal, 853, 93

Rodriguez, C. L., Amaro-Seoane, P., Chatterjee, S., & Rasio, F. A. 2018, Physical Review Letters, 120, 151101

Rodriguez, C. L., Morscher, M., Pattabiraman, B., et al. 2015, Physical Review Letters, 115, 051101

Samsing, J., & D'Orazio, D. J. 2018, Monthly Notices of the Royal Astronomical Society, 481, 5445

Samsing, J., & Ramirez-Ruiz, E. 2017, The Astrophysical Journal Letters, 840, L14

Schmidt, P., Ohme, F., & Hannam, M. 2015, Physical Review D, 91, 024043

Silsbee, K., & Tremaine, S. 2016, arXiv preprint arXiv:1608.07642

Storch, N. I., & Lai, D. 2015, Monthly Notices of the Royal Astronomical Society, 448, 1821

Wen, L. 2003, The Astrophysical Journal, 598, 419

Yu, H., Ma, S., Giesler, M., & Chen, Y. 2020, arXiv preprint arXiv:2007.12978

Ziosi, B. M., Mapelli, M., Branchesi, M., & Tormen, G. 2014, Monthly Notices of the Royal Astronomical Society, 441, 3703

Zwart, S. F. P., & McMillan, S. L. 1999, The Astrophysical Journal Letters, 528, L17